Int. J. Heat Mass Transfer. Vol. 33, No. 4, pp. 661–671, 1990
Printed in Great Britain

0017–9310/90 $3.00 + 0.00

Solidification in the presence of high Rayleigh number convection in an enclosure cooled from the side

ZONGQIN ZHANG and ADRIAN BEJAN
Department of Mechanical Engineering and Materials Science, Duke University, Durham, NC 27706, U.S.A.

(*Received* 10 *May* 1989 *and in final form* 7 *July* 1989)

Abstract—This is an experimental and theoretical study of the process of time-dependent solidification in an enclosed liquid cooled from the side. The focus is on the effect of high Rayleigh number convection, and the convection–conduction interaction across the freezing front. Experiments at $Ra \approx 10^{11}$ and $Ste \approx 0.1$ show the existence of a weakly turbulent flow in the early stages of the solidification process. The parametric domain of this study is expanded through the use of a theoretical model of the combined conduction and convection process with time-dependent stratification in the liquid pool. The accuracy of this model is demonstrated by comparing its predictions with the experimental measurements. The effect that the time, the Stefan number and the conductivity and diffusivity ratios have on the solidification rate is documented graphically.

1. INTRODUCTION

THE OBJECTIVE of this study is to document the process of time-dependent solidification in an enclosed liquid cooled from the side. The focus is on the effect of high Rayleigh number natural convection, and the complex interaction between it and the time-dependent conduction through the solidified layer. This study is the second part (the solidification aspect) of a greater effort of understanding the effect of high Rayleigh number convection on phase change processes. The first part of this effort dealt with the melting aspect [1].

The work described in this paper consists of laboratory experiments interwoven with an analytical model of the entire solidification process and its history. Our original plan was to conduct a purely experimental investigation: this is reported in Sections 3 and 4. We found, however, that the parametric domain of these experiments (e.g. Rayleigh and Stefan numbers) was restricted by the construction of the experimental apparatus.

In order to expand the domain covered by our study, we developed a theoretical treatment of the coupled conduction–convection phenomenon. This treatment is presented first (Section 2) in order to properly define the concepts and symbols that are used in both theory and experiment. Next, we demonstrate the accuracy of the theoretical model by comparing its predictions with the measurements furnished by the experiments. This series of tests forms the subject of Section 4. Finally, in Section 5, we use the theoretical model in order to cover a much wider domain of parameters such as the Rayleigh and Stefan numbers, and conductivity and thermal diffusivity ratios.

On the background of the existing literature on solidification, this experimental and theoretical study makes several contributions. On the experimental side, it documents the natural convection effect at considerably higher Rayleigh numbers, where the boundary layer flow becomes weakly turbulent. On the theoretical side, the model of Section 2 includes all the important features of the conduction–convection interaction across the freezing front. In addition to describing the natural convection boundary layer, the model includes the effect of thermal stratification in the liquid pool, and the time dependence of this stratification.

Worth noting is that earlier analytical studies of the solidification process have been simplified by avoiding the natural convection boundary layer problem and using a heat transfer coefficient on the liquid side of the interface [2–5]. In the theoretical part of this study, all the pieces of the heat transfer system are kept in the model: proceeding in the direction of higher temperatures, these are the solid layer, the natural convection boundary layer, and the thermally stratified liquid pool.

2. ANALYSIS

The model employed in the analytical part of this solidification study is shown in Fig. 1. All the walls of the enclosure except one side wall are insulated. Beginning with the time $t = 0$, the temperature of the cooled wall is lowered to and maintained at the isothermal level T_w, where $T_w < T_m$. Initially, the enclosure contains liquid with the average temperature $T_{f,i}$, such that $T_{f,i} > T_m$. Sufficiently far from the wall, the liquid is thermally stratified, $T_f(y, t)$.

The (x_1, y) system of coordinates is attached to the

NOMENCLATURE

C	instantaneous, height-averaged cooling rate (conduction into the cold wall), equation (31)
g	gravitational acceleration
h_{sf}	latent heat of fusion
H	height
k	thermal conductivity
$\tilde{L}$	dimensionless aspect ratio, equation (25)
M	instantaneous, height-averaged solidification rate, equation (29)
N	number of steps in the vertical direction, Table 1
Ra	Rayleigh number, equation (9)
s	deflection of the two-phase interface
S	volume swept by the two-phase interface, equation (30)
Ste	Stefan number (liquid superheat), equation (12)
t	time
$\Delta\tilde{t}$	time step, Table 1
T	temperature
T_m	solidification point
u	horizontal velocity component
u_0	solidification velocity, equation (15)
v	vertical velocity component
V	function, equation (5)
x	horizontal coordinate
x_1	horizontal coordinate attached to solid–liquid interface
y	vertical coordinate.

Greek symbols

α	thermal diffusivity
β	volumetric coefficient of thermal expansion
δ	thickness of liquid natural convection boundary layer
ν	kinematic viscosity
θ_s	dimensionless temperature, equation (12)
$\Delta\theta$	temperature difference, equation (7)
ρ	density of liquid or solid
ϕ	shape function, equation (19).

Subscripts

avg	average value
f	liquid
i	initial
r	ratio of solid to liquid
s	solid
w	wall.

Superscript

$(\tilde{})$	dimensionless variables defined in equations (7)–(9), (14), and (25)

solid–liquid interface ($x_1 = x - s$). In this system, the movement of the freezing front into the liquid appears as a suction velocity u_0. It is assumed further that the freezing front remains sufficiently plane and vertical over most of its height H. This assumption is valid at sufficiently short times into the solidification process, and is supported by the experiments of Section 3.

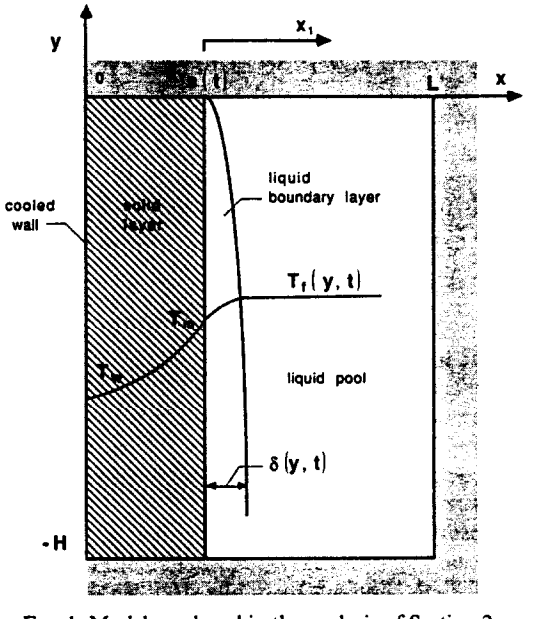

FIG. 1. Model employed in the analysis of Section 2.

The analysis is built on several additional assumptions.

(i) The liquid is Newtonian and Boussinesq incompressible.

(ii) The solid is homogeneous and isotropic.

(iii) The solid thermal conductivity and diffusivity (k_s, α_s) are not necessarily equal to the corresponding properties of the liquid (k, α). The density of the solid, however, is equal to the density of the liquid.

(iv) The solid–liquid interface is smooth.

(v) The liquid pool is linearly stratified in the vertical direction, and its bottom temperature is equal to the solidification temperature, $T_f(y = -H) = T_m$.

2.1. *The liquid-side boundary layer*

The boundary layer equations for mass, momentum and energy conservation in a liquid with Prandtl number considerably greater than 1 are

$$\frac{\partial u}{\partial x_1} + \frac{\partial v}{\partial y} = 0 \tag{1}$$

$$\nu\frac{\partial^2 v}{\partial x_1^2}+g\beta(T-T_f)=0 \tag{2}$$

$$\frac{\partial T}{\partial t}+\frac{\partial}{\partial x_1}(uT)+\frac{\partial}{\partial y}(vT)=\alpha\frac{\partial^2 T}{\partial x_1^2}. \tag{3}$$

These equations were solved based on the integral method, by assuming Squire profiles [6]

$$T=T_f-\Delta T_f\left(1-\frac{x_1}{\delta}\right)^2 \tag{4}$$

$$v=V\frac{x_1}{\delta}\left(1-\frac{x_1}{\delta}\right)^2 \tag{5}$$

in which $\Delta T_f=T_f-T_m$, and T_f, V and the boundary layer thickness δ are all functions of time (t) and altitude (y). The integral analysis is standard, and is omitted for the sake of brevity. Its final product is the equation

$$\frac{2}{3}\tilde{\delta}\frac{\partial}{\partial\tilde{t}}(\Delta\theta)-\frac{1}{3}\Delta\theta\frac{\partial\tilde{\delta}}{\partial\tilde{t}}+\Delta\theta\tilde{u}_0-\frac{1}{90}\frac{\partial}{\partial\tilde{y}}(\Delta\theta^2\tilde{\delta}^3)+2\frac{\Delta\theta}{\tilde{\delta}}=0 \tag{6}$$

in which the dimensionless variables are defined as follows:

$$\Delta\theta=\frac{T_f-T_m}{T_{f,i}-T_m},\quad \tilde{y}=-\frac{y}{H} \tag{7}$$

$$\tilde{\delta}=\frac{\delta}{H}Ra^{1/4},\quad \tilde{u}_0=u_0\frac{H}{\alpha}Ra^{-1/4} \tag{8}$$

$$\tilde{t}=t\frac{\alpha}{H^2}Ra^{1/2},\quad Ra=\frac{g\beta(T_{f,i}-T_m)H^3}{\alpha\nu}. \tag{9}$$

2.2. *The interface condition*

The conservation of energy at the solid–liquid interface requires

$$\rho h_{sf}\frac{ds}{dt}=k_s\left.\frac{\partial T_s}{\partial x}\right|_{x=s}-k_f\left.\frac{\partial T}{\partial x_1}\right|_{x_1=0} \tag{10}$$

where h_{sf} is the latent heat of solidification, and $s(t)$ the thickness of the solid layer (Fig. 1). A dimensionless alternative to this equation is

$$\frac{1}{Ste}\frac{d\tilde{s}}{d\tilde{t}}=k_rT_r\left.\frac{\partial\theta_s}{\partial\tilde{x}}\right|_{\tilde{x}=\tilde{s}}-\frac{2\Delta\theta}{\tilde{\delta}} \tag{11}$$

to which the following definitions apply:

$$Ste=\frac{c(T_{f,i}-T_m)}{h_{sf}},\quad \theta_s=\frac{T_s-T_w}{T_m-T_w} \tag{12}$$

$$k_r=\frac{k_s}{k},\quad T_r=\frac{T_m-T_w}{T_{f,i}-T_m} \tag{13}$$

$$\tilde{s}=\frac{s}{H}Ra^{1/4},\quad \tilde{x}=\frac{x}{H}Ra^{1/4}. \tag{14}$$

The relationship between the interface position and the suction velocity of the liquid-side boundary layer is

$$\frac{d\tilde{s}}{d\tilde{t}}=-\tilde{u}_0. \tag{15}$$

2.3. *The solid layer*

In terms of the dimensionless variables defined above, the phenomenon of time-dependent conduction in the solid layer is described by

$$\frac{\partial\theta_s}{\partial\tilde{t}}=\alpha_r\frac{\partial^2\theta_s}{\partial\tilde{x}^2} \tag{16}$$

$$\theta_s=0\quad \text{at}\ \tilde{x}=0 \tag{17a}$$

$$\theta_s=1\quad \text{at}\ \tilde{x}=\tilde{s} \tag{17b}$$

where α_r is the thermal diffusivity ratio

$$\alpha_r=\frac{\alpha_s}{\alpha_f}. \tag{18}$$

This problem was solved using the integral method described by Goodman [7], which begins with assuming for $\tilde{\theta}_s$ a polynomial expression that satisfies the boundary conditions

$$\tilde{\theta}_s=\phi(\tilde{t})\frac{\tilde{x}}{\tilde{s}}+\left[1-\phi(\tilde{t})\right]\left(\frac{\tilde{x}}{\tilde{s}}\right)^2. \tag{19}$$

Differentiating equation (17b) with respect to the time $\tilde{t}$ at $\tilde{x}=\tilde{s}$ yields

$$\left.\frac{\partial\theta_s}{\partial\tilde{x}}\right|_{\tilde{x}=\tilde{s}}\frac{d\tilde{s}}{d\tilde{t}}+\left.\frac{\partial\theta_s}{\partial\tilde{t}}\right|_{\tilde{x}=\tilde{s}}=0. \tag{20}$$

The derivatives $d\tilde{s}/d\tilde{t}$ and $\partial\theta_s/\partial\tilde{t}$ can be eliminated between equations (20), (16) and (11). Substituting into the resulting equation the $\tilde{\theta}_s$ profile (19) leads finally to

$$\frac{1}{Ste}\frac{d\tilde{s}}{dt}=\frac{k_rT_r}{\tilde{s}}(2-\phi)-\frac{2\Delta\theta}{\tilde{\delta}} \tag{21}$$

in which

$$2-\phi=\left\{2\,Ste\frac{\tilde{s}\Delta\theta}{\tilde{\delta}}-2\alpha_r+\left[\left(2\,Ste\frac{\tilde{s}\Delta\theta}{\tilde{\delta}}-2\alpha_r\right)^2+8\,Ste\,k_rT_r\alpha_r\right]^{1/2}\right\}\Big/(2\,Ste\,k_rT_r). \tag{22}$$

2.4. *The liquid pool*

The conservation of energy in the entire space occupied by liquid requires

$$\rho c\int_0^H\int_0^\delta\frac{\partial T}{\partial t}dx_1\,dy+\rho c\int_0^H\int_\delta^{L-s}\frac{\partial T_f}{\partial t}dx_1\,dy=-\int_0^H k_f\left.\frac{\partial T}{\partial x_1}\right|_{x_1=s}dy. \tag{23}$$

The dimensionless counterpart of this condition is

$$\left(\tilde{L}-\tilde{s}-\frac{\tilde{\delta}}{3}\right)\frac{\partial\Delta\theta}{\partial\tilde{t}}=-2\frac{\Delta\theta}{\tilde{\delta}}+\frac{\Delta\theta}{3}\frac{\partial\tilde{\delta}}{\partial\tilde{t}} \tag{24}$$

where

$$\tilde{L} = \frac{L}{H} Ra^{1/4}. \quad (25)$$

In summary, the model is almost the same as the one we used with considerable success in the earlier phase of this project, in which we dealt with the process of melting at high Rayleigh numbers [1]. The new feature of the present model is the time-dependent, linear vertical stratification that is assumed to exist in the liquid pool. This feature is new also relative to the solidification models that have been published [2–5]. The liquid vertical stratification was assumed linear throughout the solidification process because (i) experience with quasi-steady natural convection in liquids cooled from the side shows that the 'core' is practically linearly stratified, and (ii) the experimental temperature measurements of Fig. 6 confirm that this is a reasonable, engineering assumption.

2.5. *Solution*

In summary, the analysis resulted in four equations—equations (6), (21), (22) and (24)—which contain four unknowns, $\tilde{\delta}$, $\Delta\theta$, $\tilde{s}$ and ϕ. The physical system is characterized by five dimensionless groups, namely *Ste*, $\tilde{L}$, k_r, T_r and α_r. The initial and boundary conditions are

$$\Delta\theta = 1, \quad \tilde{s} = 0, \quad \tilde{\delta} = 0 \quad \text{at } \tilde{t} = 0 \quad (26)$$

$$\tilde{\delta} = 0 \quad \text{at } \tilde{y} = 0 \quad (27)$$

$$\frac{\partial \Delta\theta}{\partial \tilde{y}} = 0 \quad \text{at } \tilde{y} = 0 \text{ and } \tilde{y} = 1. \quad (28)$$

The problem summarized above was solved numerically. Equation (6) was solved by the Euler implicit method, and the remaining equations by the first-order explicit method. The accuracy of the numerical method is documented in Table 1, which shows the freezing front position $\tilde{s}$ at two particular times ($\tilde{t} = 0.5$ and 50), and at three vertical locations ($\tilde{y} = 0.05$, 0.5 and 0.95). The vertical interval $0 \leqslant \tilde{y} \leqslant 1$ was divided into $N-1$ steps. The numerical values listed in the table show that the use of the time step $\Delta\tilde{t} = 0.01$ and $N = 41$ leads to a solution that is insensitive to the fineness of the grid. The numerical solutions described in what follows are all based on $\Delta\tilde{t} = 0.01$ and $N = 41$.

The behavior of the time-dependent freezing process was monitored by calculating the instantaneous total solidification rate

$$M(\tilde{t}) = \frac{1}{Ste} \int_0^1 \frac{d\tilde{s}}{d\tilde{t}} d\tilde{y} \quad (29)$$

and the instantaneous volume (frontal area in Fig. 1) occupied by the solidified material

$$S(\tilde{t}) = \int_0^{\tilde{t}} M(\tilde{t})\, d\tilde{t}. \quad (30)$$

Another dimensionless aggregate quantity of interest is the instantaneous cooling rate, or the total heat transfer rate from the solid layer to the side wall of temperature T_w

$$C(\tilde{t}) = k_r T_r \int_0^1 \frac{\phi}{\tilde{s}} d\tilde{y}. \quad (31)$$

The average dimensionless temperature of the liquid pool is a decaying function of time

$$\Delta\theta_{avg}(\tilde{t}) = \int_0^1 \Delta\theta(\tilde{t}, \tilde{y})\, d\tilde{y}. \quad (32)$$

3. EXPERIMENTAL APPARATUS

Solidification experiments were conducted in a rectangular test cell the construction of which is described in great detail in an earlier study of melting in the presence of natural convection [1]. Figure 2 shows the experimental cavity, which has a height of 74 cm, a width of 14.6 cm, and a depth (normal to the plane of the figure) of 56 cm. The two large side walls are made out of 1.8 cm thick aluminum plate. One of these can be cooled by circulating a stream of water or alcohol supplied by a constant-temperature bath system.

The 56 cm depth of the enclosure was chosen in order to minimize the three-dimensional characteristics of the circulation in the liquid zone. When judging the size of this dimension (the depth), it is important not to compare it with the 14.6 cm width

Table 1. The effect of the time step ($\Delta\tilde{t}$) and the number of grid points in the vertical direction (N) on the position of the solid–liquid interface, $\tilde{s}$ (*Ste* = 0.1, T_r = 1.175, k_r = 2.355, α_r = 2.74, $\tilde{L}$ = 100)

	$\tilde{t} = 0.5$			$\tilde{t} = 50$				
y =	0.05	0.5	0.95	0.05	0.5	0.95	N	$\Delta\tilde{t}$
$\tilde{s}$	0.3765	0.3848	0.3904	2.615	3.248	3.514	21	0.1
	0.3828	0.3907	0.3955	2.616	3.261	3.515	31	0.01
	0.3841	0.3907	0.3955	2.628	3.257	3.514	41	0.01
	0.3847	0.3912	0.3960	2.629	3.258	3.515	41	0.001

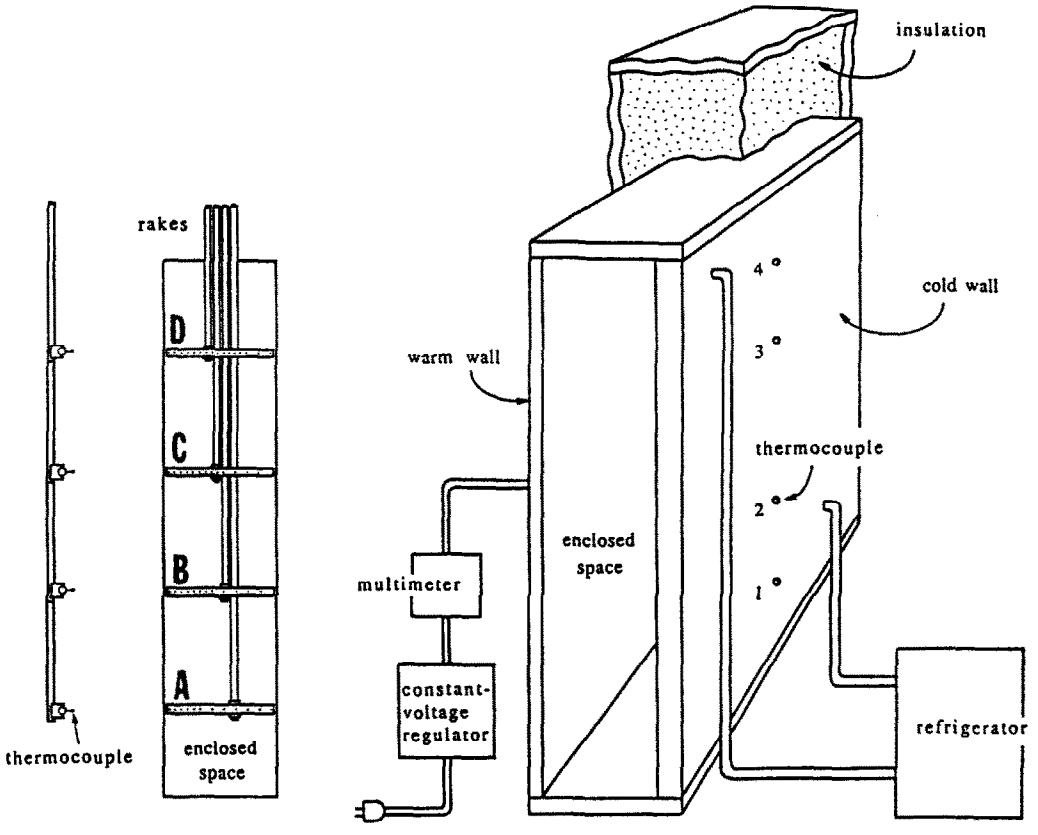

FIG. 2. Scale drawing of the experimental apparatus and its instrumentation.

of the box, because this width is not the proper length scale of the flow. The proper transversal length scale of the flow is the thickness of the vertical boundary layer, which in the high *Ra* range of this experiment is of the order of only a few millimeters. The depth of the box is therefore two orders of magnitude larger than the transversal length scale of the flow, and, as a consequence, the boundary layer circulation is practically two-dimensional. The two-dimensionality of the flow is reflected also in the nearly plane shape of the solid–liquid interface, as noted at the end of this section.

The remaining walls of the enclosure are made out of 2.5 cm thick acrylic plexiglas sheet. The enclosure is surrounded by a 15 cm thick layer of fiberglass insulation. The phase-change material (paraffin) used inside the cavity is research grade (99% pure) n-octadecane, with a melting point $T_m = 28°C$. Before each experimental run, the liquid paraffin in the test cavity was preheated to a steady, nearly uniform temperature. This procedure lasted approximately 10–14 h.

Each experimental run was initiated by circulating a stream of cold water of preset temperature through the hollow back of the aluminum side wall. The desired initial temperature condition was achieved only after approximately 20–30 min, because of the thermal inertia effect of the aluminum wall. The initial temperature distribution in the liquid was not perfectly uniform: the temperature difference between the top and bottom of the cavity was roughly 2°C, and the temperature variation in the transversal direction was approximately 0.5°C. These temperature variations were monitored with the thermocouple rakes that are described next.

The temperature distribution along the two side walls were measured by means of thermocouples positioned at four altitudes (labeled 1, 2, 3 and 4) in the vertical midplane of the apparatus. The temperature history in the solid and liquid regions was monitored with 55 chromel–alumel (type K) thermocouples held by four horizontal rakes (labeled A, B, C and D in Fig. 2). The rakes were made out of acrylic plexiglas rod.

The shape of the solid–liquid interface was photographed at several instances during the solidification process. The volume or frontal area of the solid region was measured graphically on enlargements of the photographs. The volume-measuring accuracy of this method is 1.5%, as demonstrated by special tests reported in ref. [1]. The chief parameters of the experiments conducted in this study are summarized in Table 2.

Table 2. Physical parameters of the solidification experiments conducted in this study, and the corresponding dimensionless groups used in the model of Section 2

Run	$T_{f,i}$ (°C)	$T_{w,avg}$ (°C)	Ra	Ste	$\tilde{L}$	k_r	T_r	z_r
1	36.1	19.0	5.39×10^{10}	0.072	107.0	2.36	1.141	2.74
2	44.9	18.1	1.13×10^{11}	0.15	121.2	2.36	0.585	2.74
3	35.7	18.8	5.11×10^{10}	0.068	99.4	2.36	1.175	2.74

Figure 3 shows a sequence of photographs of the solid–liquid interface. For better orientation, the thickness of the solid layer is highlighted with a pair of arrowheads: this thickness increases slightly downward. Early in the solidification process, the interface–liquid temperature difference is large (Ra is of the order of 10^{10}–10^{11}), and the flow is weakly turbulent along the freezing front. The long waves and sluggish fluctuations of the flow were visible as shadows on the freezing front, while looking at it at a 45° angle.

The waviness was similar to what we learned to associate with the early transition region in a boundary layer flow. There was no sign of intense eddy motion that would suggest that the flow departed significantly from the laminar regime. For this reason, the quantitative solidification results obtained experimentally are directly comparable with the results of the laminar-flow model of Section 2. After all, in vertical boundary layer natural convection the laminar-flow heat transfer correlation works very well throughout the region of transition to turbulent flow.

During the late stages, the liquid temperature approaches the solidification point T_m, and dendritic formations grow at the interface. In general terms, the solid–liquid interface is nearly plane and vertical throughout the solidification process [3, 8]. Based on our experimental observations, we feel that the curvature of the interface was negligible throughout the solidification run, and never invalidated the model described in Section 2.

Worth noting is that in some solidification experiments involving cooled vertical tubes [8, 9], the slope of the solid–liquid interface was somewhat larger than in the present experiments. The difference is due to the cylindrical shape of the vertical-tube geometry, which accentuates the thermal resistance posed by the

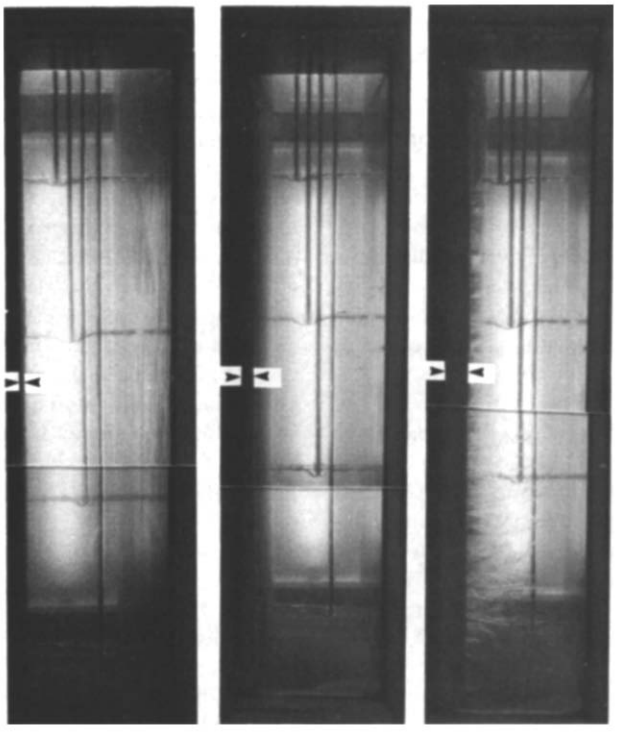

FIG. 3. Sequence of photographs showing the evolution of the two-phase interface ($Ra = 5.39\times10^{10}$: from left to right, the elapsed times were 45, 95 and 245 min).

solid layer when it becomes thick at the bottom, and in this way accentuates the slope of the freezing front relative to the tube wall.

4. EXPERIMENTAL RESULTS

Figures 4(a) and (b) show the experimental values of the average liquid temperature

$$T_{f,avg} = \frac{1}{H(L-s)} \int_0^H \int_s^L T \, dx \, dy \qquad (33)$$

and the frozen fraction of the cavity volume, s_{avg}/L. The thickness s_{avg} is the H-averaged value of the instantaneous thickness of the frozen layer. The value of the integral on the right-hand side of equation (33) was calculated by properly averaging all the readings provided by the thermocouple rakes. In a single rake (i.e. in the horizontal direction), the differences between the temperature readings were negligible, therefore these readings were averaged arithmetically. In the vertical direction, the average readings provided by the four rakes were first curve-fitted, and the resulting expression was then integrated according to equation (33).

Figures 4(a) and (b) show also the corresponding curves provided by the theoretical model described in Section 2, in which the present experiments are represented by the Ste, $\tilde{L}$, k_r and α_r values displayed in Table 2. The agreement between experimental

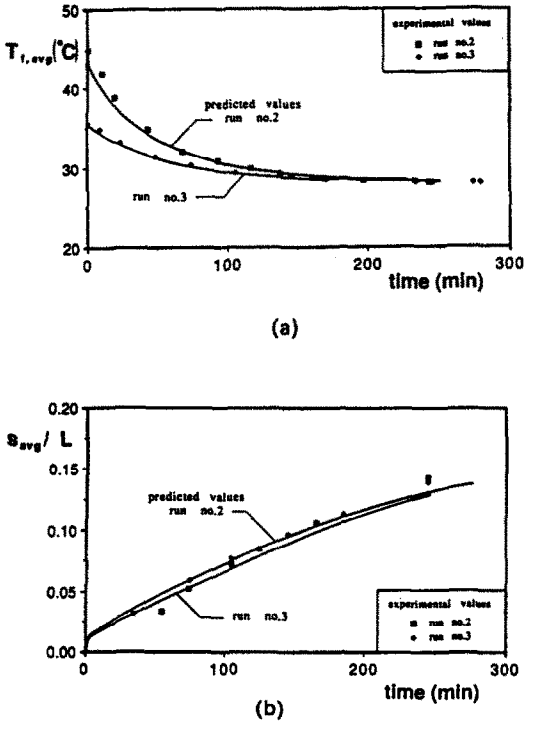

FIG. 4. The average liquid pool temperature (a) and the volume of the solid (b): experimental measurements vs theoretical predictions.

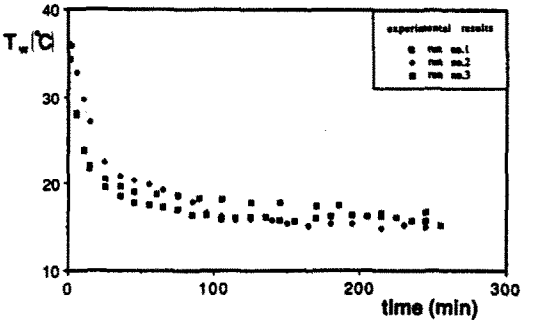

FIG. 5. The history of the temperature of the cooled side wall.

measurements and numerical calculations is very good. Some disagreement is evident in the small-time limit, because in that range the thermal inertia of the wall prevents the establishment of a true constant-temperature wall condition. The history of the measured wall temperature is reported in Fig. 5.

The average temperature measured along the vertical direction is shown in Figs. 6(a) and (b). The curves recommended by the model of Section 2 are shown also. The agreement between experiment and numerical calculations is very good, especially in the late stages of the solidification process. Less satisfactory is the agreement registered in the small-time limit at $\tilde{y}$ levels near the bottom of the liquid pool. This is due to the fact that in the experiment the initial liquid-pool temperature $T_{f,i}$ is constant, i.e. higher than the solidification point T_m at all $\tilde{y}$'s. A certain time is required in order for the natural convection loop to generate enough T_m-cold liquid that settles at the bottom of the pool.

Figure 7 shows the measured distribution of temperature in the horizontal direction, that is across the cavity. The horizontal bars indicate the corresponding temperature levels predicted by analysis. Good agreement is registered between the measurements and the vertical stratification function $T_f(y)$ calculated with the model of Section 2. The three time frames of Fig. 7 show that, indeed, the liquid pool temperature approaches the solidification point (28°C) as the time increases, and as the effect of natural convection subsides. The figure shows also that the modeling assumption that the liquid pool temperature is not a function of x (assumption (v) in Section 2) is justified.

5. DISCUSSION

The purpose of the results discussed until now was to verify the validity of the theoretical model constructed in Section 2. The objective of the remaining figures is to use the model in order to cover a much wider parametric domain than the one documented by the experiments of Table 2.

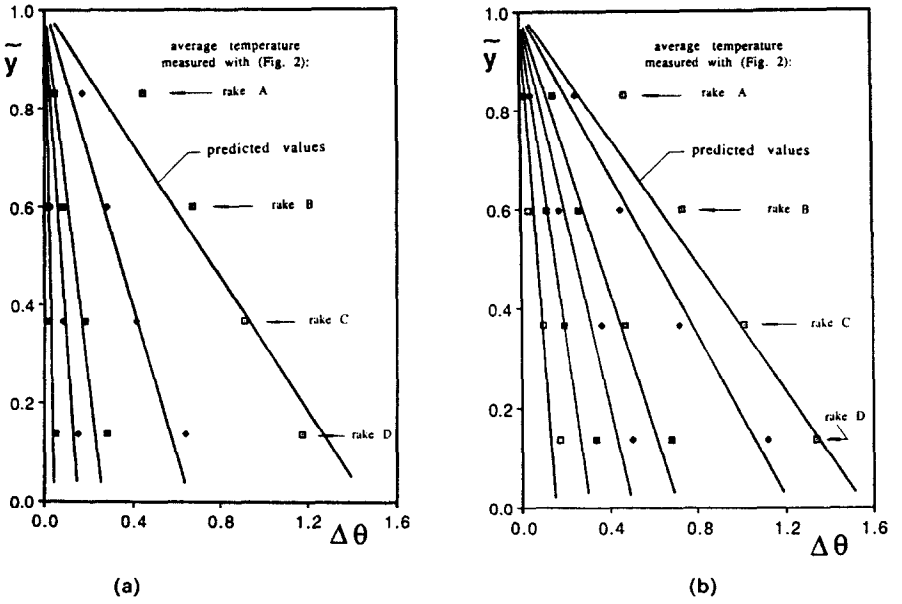

FIG. 6. The average temperature distribution along the vertical direction in (a) run No. 2 and (b) run No. 3: experimental measurements vs theoretical predictions.

Figures 8(a), (b) and 9(a), (b) present the effect of the Stefan number *Ste* on the instantaneous solidification rate, $M(\tilde{t})$, the volume swept by the freezing front, $S(\tilde{t})$, the instantaneous cooling rate through the side wall, $C(\tilde{t})$, and the average liquid temperature, $\Delta\theta_{avg}(\tilde{t})$. Figure 9 shows that the average liquid temperature begins a steep descent towards zero as $\tilde{t}$ exceeds $O(10^2)$. The Stefan number has only a weak effect on the liquid pool temperature.

The solidification rate shown in Fig. 8(a) decreases significantly as the Stefan number increases. It also decreases as the time $\tilde{t}$ increases, i.e. as the effect of natural convection dies down. These trends are visible also in Fig. 8(b), where the solid volume $S(\tilde{t})$ is the time integral of the instantaneous solidification rate $M(\tilde{t})$, equation (30).

The cooling rate curves $C(\tilde{t})$ of Fig. 9(a) repeat the features of the solidification rate curves $M(\tilde{t})$ of Fig.

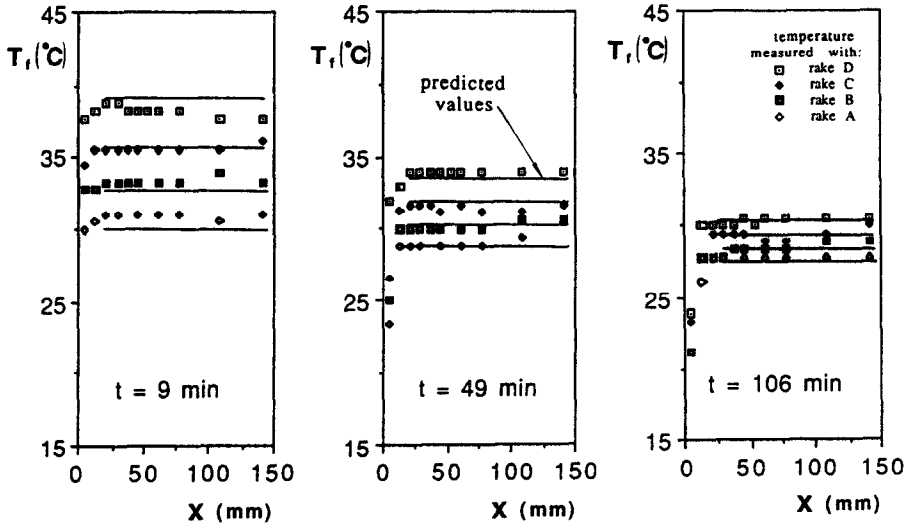

FIG. 7. The temperature distribution in the horizontal direction through the cavity: experimental measurements vs theoretical predictions.

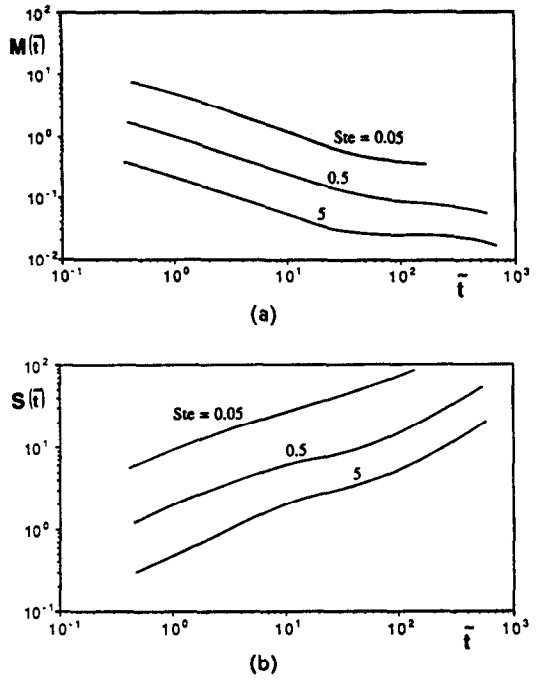

FIG. 8. The effect of the Stefan number on the solidification rate (a) and the solid inventory (b) ($k_r = 2.355$, $\alpha_r = 2.74$, $T_r = 1$, $\tilde{L} = 100$).

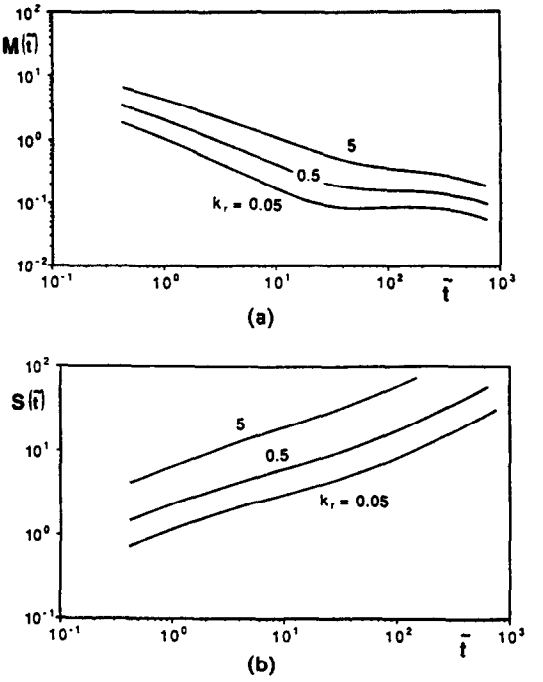

FIG. 10. The effect of the thermal conductivity ratio on the solidification rate (a) and the solid inventory (b) ($Ste = 0.1$, $\alpha_r = 1$, $\tilde{L} = 100$, $T_r = 1$).

8(a). This time, however, the *Ste* effect is considerably less pronounced than in Fig. 8(a).

The effect of the transport-property ratios k_r and α_r is illustrated in Figs. 10(a), (b) and 11(a), (b). A higher conductivity ratio k_r (i.e. a solid that is more conductive than its liquid phase) will have a relatively larger solidification rate (Fig. 10(a)) and solid volume inventory (Fig. 10(b)). The thermal diffusivity ratio α_r has a less pronounced effect.

The effect of the horizontal dimension of the

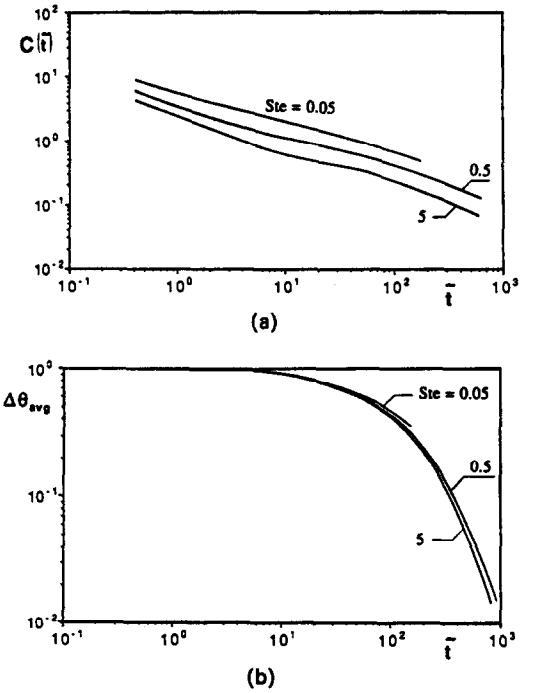

FIG. 9. The effect of the Stefan number on the heat transfer rate through the cooled wall (a) and the average liquid temperature (b) ($k_r = 2.355$, $\alpha_r = 2.74$, $T_r = 1$, $\tilde{L} = 100$).

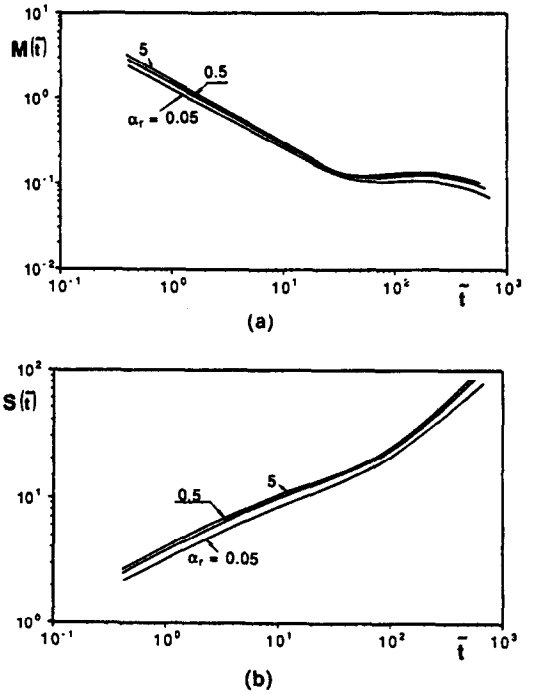

FIG. 11. The effect of the thermal diffusivity ratio on the solidification rate (a) and the solid inventory (b) ($Ste = 0.1$ $k_r = 1$, $\tilde{L} = 100$, $T_r = 1$).

cavity, $\tilde{L}$, is documented in Figs. 12(a) and (b). This length scale (the thickness of the initial pool of liquid) has a negligible effect in early stages of the solidification process, when the solid layer is much thinner than the liquid cavity. The effect of $\tilde{L}$ is sizeable in the long-time limit, where both the melting rate and the solid inventory decrease as $\tilde{L}$ increases. Worth noting is the peculiar shape achieved by the $M(\tilde{t})$ curve of Fig. 12(a) as $\tilde{L}$ and $\tilde{t}$ increase: this 'van der Waals gas' shape is similar to that of the instantaneous heat transfer rate curves observed in experiments of natural convection-assisted melting [10].

Figures 13(a), (b) and 14(a), (b) document the effect of the temperature difference ratio T_r, equation (13). The instantaneous solidification rate $M(\tilde{t})$ increases by a factor of order 10 as T_r increases by a factor of 10^2. The same effect is exhibited by the instantaneous solid inventory (Fig. 13(b)), and by the instantaneous heat transfer rate through the side wall on which the solid layer forms (Fig. 14(a)). The T_r ratio has practically no effect on the average temperature of the liquid pool (Fig. 14(b)).

Looking back at the origin of the preceding results, the model on which the analytical and numerical part of the paper is based applies only to liquids with Prandtl numbers greater than 1. This restriction can be relaxed by including the missing inertia terms in the momentum equation (2), and redoing the subsequent analysis. This more general model will exhibit the

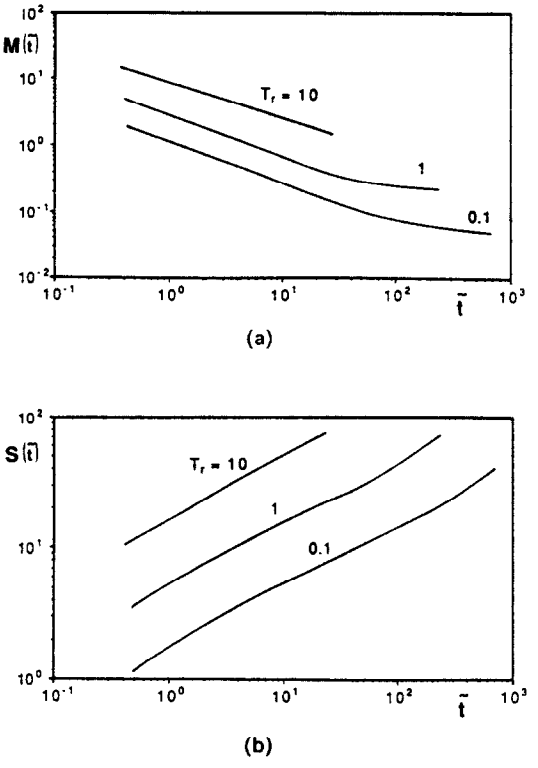

FIG. 13. The effect of the subcooling/superheating ratio T_r on the solidification rate (a) and the solid inventory (b) ($Ste = 0.1$, $k_r = 2.355$, $\alpha_r = 2.74$, $\tilde{L} = 100$).

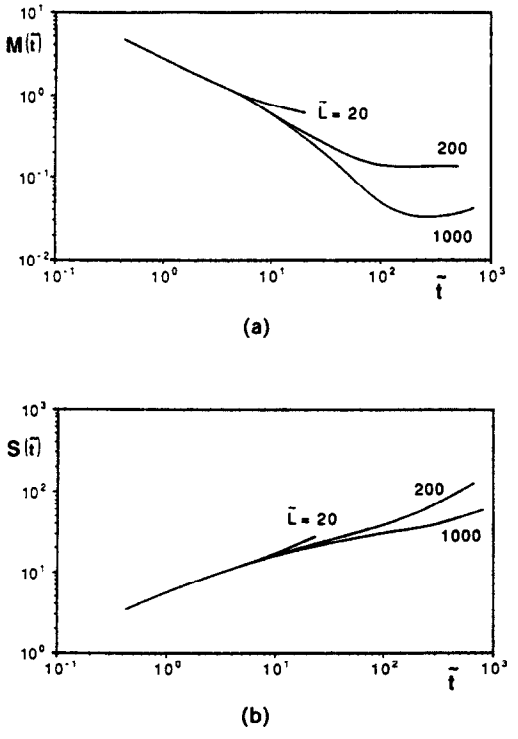

FIG. 12. The effect of the horizontal dimension of the cavity on the solidification rate (a) and the solid inventory (b) ($Ste = 0.1$, $k_r = 2.355$, $\alpha_r = 2.74$, $T_r = 1$).

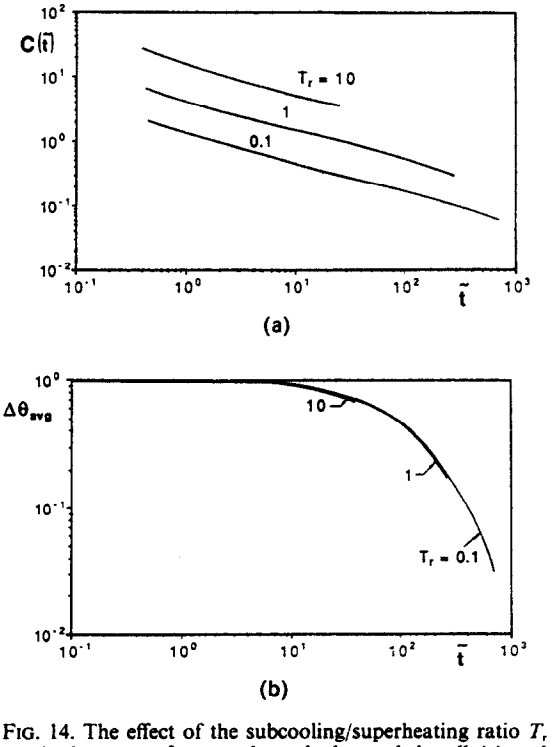

FIG. 14. The effect of the subcooling/superheating ratio T_r on the heat transfer rate through the cooled wall (a) and the average liquid temperature (b) ($Ste = 0.1$, $k_r = 2.355$, $\alpha_r = 2.74$, $\tilde{L} = 100$).

Prandtl number as an additional dimensionless group, next to the five groups contained already in the present model (Ste, $\tilde{L}$, k_r, T_r, α_r). In this paper, we chose a model applicable to the $Pr > 1$ range because (i) the paraffin used in the experiment has a large Pr value (namely, $Pr = 52$), and (ii) we sought to minimize the total number of dimensionless groups.

Acknowledgement—This work was supported by the Electric Power Research Institute through contract No. RP 8006-4, under the management of Dr Jong H. Kim.

REFERENCES

1. Z. Zhang and A. Bejan, Melting in an enclosure heated at constant rate, *Int. J. Heat Mass Transfer* **32**, 1063–1076 (1989).
2. J. Szekely and P. S. Chhabra, The effect of natural convection on the shape and movement of the melt–solid interface in the controlled solidification of lead, *Metall. Trans.* **1**, 1195–1203 (1970).
3. A. G. Bathelt and R. Viskanta, Heat transfer at the solid–liquid interface during melting from a horizontal cylinder, *Int. J. Heat Mass Transfer* **23**, 1493–1503 (1980).
4. N. W. Hale, Jr. and R. Viskanta, Solid–liquid phase-change heat transfer and interface motion in materials cooled or heated from above or below, *Int. J. Heat Mass Transfer* **23**, 283–292 (1980).
5. C. Gau and R. Viskanta, Melting and solidification of a metal system in a rectangular cavity, *Int. J. Heat Mass Transfer* **17**, 113–123 (1984).
6. H. B. Squire, Integral solution published in *Modern Developments in Fluid Dynamics* (Edited by S. Goldstein), Vol. 2, pp. 641–643. Dover, New York (1965).
7. T. R. Goodman, Application of integral methods to transient nonlinear heat transfer. In *Advances in Heat Transfer* (Edited by T. F. Irvine, Jr. and J. P. Hartnett), Vol. 1, pp. 51–122. Academic Press, New York (1964).
8. E. M. Sparrow, J. W. Ramsey and J. S. Harris, The transition from natural-convection-controlled freezing to conduction-controlled freezing, *J. Heat Transfer* **103**, 7–12 (1981).
9. M. H. Chun, H. O. Choi, H. G. Jun and Y. S. Kim, Phase-change front prediction by measuring the wall temperature on which solidification occurs, *Int. J. Heat Mass Transfer* **30**, 2641–2650 (1987).
10. B. W. Webb and R. Viskanta, On the characteristic length scale for correlating melting heat transfer data, *Int. Commun. Heat Mass Transfer* **12**, 637–646 (1985).

SOLIDIFICATION EN PRESENCE D'UNE CONVECTION A FORT NOMBRE DE RAYLEIGH DANS UNE CAVITE REFROIDIE LATERALEMENT

Résumé—C'est une étude expérimentale et théorique du mécanisme de la solidification d'un liquide enfermé et refroidi latéralement. On s'intéresse à l'effet de la convection à grand nombre de Rayleigh et de l'interaction convection–conduction à travers le front de congélation. Des expériences à $Ra = 10^{11}$ et $Ste = 0{,}1$ montre l'existence d'un écoulement faiblement turbulent dans les premiers stades du mécanisme de solidification. Le domaine paramétrique de cette étude est développé par utilisation d'un modèle théorique de la conduction mélée à la convection avec stratification variable dans le bain liquide. La précision de ce modèle est montrée par la comparaison de ses résultats et des mesures expérimentales. On montre graphiquement l'effet sur la solidification du temps, du nombre de Stefan et des rapports des conductivités et des diffusivités.

ERSTARRUNGSVORGÄNGE IN EINEM SEITLICH GEKÜHLTEN HOHLRAUM BEI KONVEKTION MIT HOHER RAYLEIGH-ZAHL

Zusammenfassung—Der zeitabhängige Erstarrungsvorgang in einer eingeschlossenen, seitlich gekühlten Flüssigkeit wird experimentell und theoretisch untersucht. Der Schwerpunkt liegt auf der Beschreibung der Konvektion mit hoher Rayleigh-Zahl und der gegenseitigen Beeinflussung von Konvektion und Wärmeleitung an der Gefrierfront. Die Experimente bei $Ra \approx 10^{11}$ und $Ste \approx 0{,}1$ zeigen die Existenz einer schwachen turbulenten Strömung im frühen Stadium des Erstarrungsvorgangs. Die Parameterstudie wurde durch die Verwendung eines theoretischen Modells erweitert, in dem kombinierte Wärmeleitung und Konvektion mit zeitabhängiger Schichtung in der Flüssigkeit berücksichtigt wird. Die Genauigkeit des Modells wird durch den Vergleich der Rechenergebnisse mit Meßwerten bestätigt. Der Einfluß von Zeit, Stefan-Zahl, Wärmeleitungs- und Diffusivitätsverhältnis auf den Erstarrungsvorgang wird grafisch dargestellt.

ВЛИЯНИЕ КОНВЕКЦИИ НА ПРОЦЕСС ЗАТВЕРДЕВАНИЯ ЖИДКОСТИ В ОХЛАЖДАЕМОЙ СБОКУ ПОЛОСТИ ПРИ БОЛЬШИХ ЧИСЛАХ РЭЛЕЯ

Аннотация—Экспериментально и теоретически исследуется нестационарное затвердевание в замкнутом объеме жидкости, охлаждаемой сбоку. Особое внимание уделяется влиянию конвекции при больших чихлах Рэлея, а также взаимодействию эффектов конвекции и теплопроводности на положение фронта замораживания. В экспериенах, проведенных при $Ra \approx 10^{11}$ и $Ste \approx 0{,}1$, обнаружено существование слабо турбулентного течения на ранних стадиях процесса. Область параметров расширена при помощи теоретической модели связанного процесса теплопроводности и конвекции с нестационарной стратификацией в объеме жидкости. Адекватность данной модели оценивается сравнением расчетов с экспериментальными данными. Графически показано влияние времени, числа Стефана, а также соотношения коэффициентов теплопроводности и температуропроводности на скорость затвердевания.